Coherence analysis of geophysical wakes in flow past a three-dimensional hill

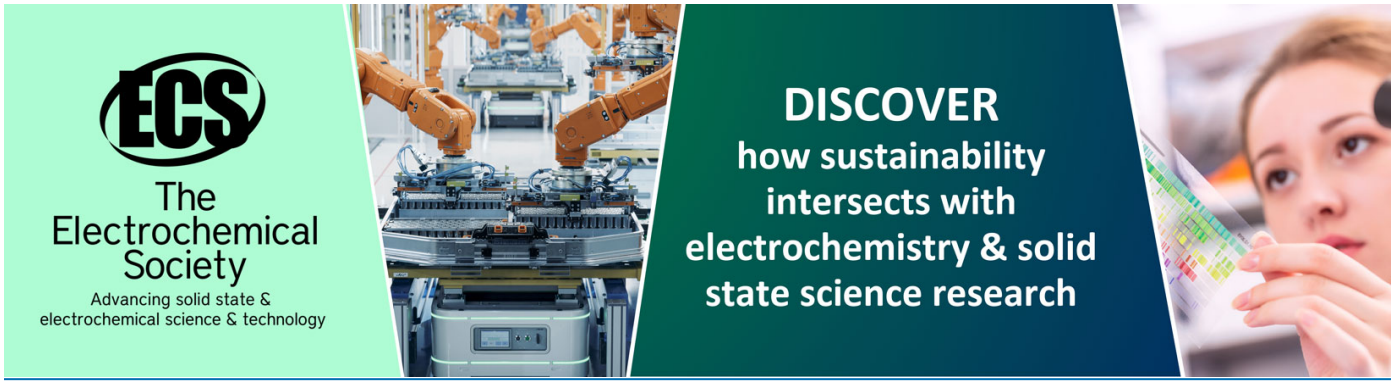

Coherence analysis of geophysical wakes in flow past a three-dimensional hill

Jinyuan Liu[1] **and Sutanu Sarkar**[1,2]

[1]Department of Mechanical and Aerospace Engineering, UC San Diego, La Jolla, CA 92093, USA

[2]Scripps Institution of Oceanography, La Jolla, CA 92037, USA

E-mails: jinyuanliu@ucsd.edu, ssarkar@ucsd.edu

Abstract. Wakes generated by topographies are ubiquitous in nature. The formation and evolution mechanism of wake-generated eddies is essential to understanding the effect of topography on oceanic bottom flow. In this study, we analyze the temporally resolved numerical database [1] of stratified wakes past an isolated three-dimensional hill, via proper orthogonal decomposition (POD) of the vertical vorticity field. We study the dynamics of the near wake ($x/D < 3$) and the far wake ($x/D \geq 3$) separately, where x is the downstream distance from the center of the hill. The aim is to understand how rotation influences the change of coherence from the near to the far wake and also the coherence across heights.

1. Introduction and motivation

Eddies are found everywhere in the ocean and the atmosphere and their origins are diverse. In this work we focus on eddies generated by a known source - an isolated seamount in deep water. Figure 1 illustrates the physical setting. A conical hill with base diameter D and height $h = 0.3D$ on the bottom of the seafloor interacts with a steady current with velocity U_∞ in the x-direction. The background density is linearly stratified and the reference frame is rotating at a frequency of $\Omega_c = f_c/2$, where f_c is the Coriolis frequency.

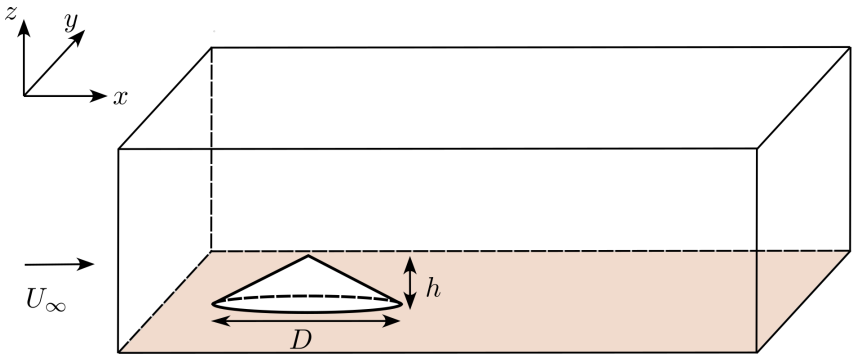

Figure 1: Flow configuration.

We use a temporally resolved LES database [1]. The flow is governed by the incompressible

Navier-Stokes equations under the Boussinesq approximation:

$$\nabla \cdot \boldsymbol{u} = 0 \tag{1}$$

$$\frac{\partial \boldsymbol{u}}{\partial t} + \nabla \cdot (\boldsymbol{u}\boldsymbol{u}) + f_c \hat{\boldsymbol{e}}_z \times (\boldsymbol{u} - U_\infty \hat{\boldsymbol{e}}_x) = -\frac{1}{\rho_0}\nabla p^* + \nabla \cdot \boldsymbol{\tau} - \frac{\rho^* g}{\rho_0}\hat{\boldsymbol{e}}_z \tag{2}$$

$$\frac{\partial \rho}{\partial t} + \nabla \cdot (\rho \boldsymbol{u}) = \nabla \cdot \boldsymbol{J}_\rho \tag{3}$$

where the stress and the scalar flux are

$$\boldsymbol{\tau} = (\nu + \nu_{\text{sgs}})(\nabla \boldsymbol{u} + \boldsymbol{u}\nabla),\ \boldsymbol{J}_\rho = (\kappa + \kappa_{\text{sgs}})\nabla\rho, \tag{4}$$

with ν being the kinematic viscosity and κ being the scalar (density) diffusivity. The sub-grid scales (denoted by subscript 'sgs') are estimated with the WALE model [2]. Here $\boldsymbol{u} = (u, v, w)$ is the velocity vector in (x, y, z) directions, p is pressure, and ρ is density. Unit vectors $\hat{\boldsymbol{e}}_x$ and $\hat{\boldsymbol{e}}_z$ are in x and z directions, respectively. The pressure and density involved in the momentum equations (2) are their deviations (p^* and ρ^*) from the hydrostatic balance, where a vertical pressure gradient balances the unperturbed background density field, and the geostrophic balance, where a spanwise pressure gradient balances the Coriolis force due to the uniform freestream. The equations are solved with a central finite-difference solver on a Cartesian grid and the object is handled with an immersed boundary method [3, 4]. For more numerical details the readers are referred to [5, 1].

Table 1 gives a summary of the simulation parameters. The flow is controlled by the following non-dimensional numbers: the rotation Rossby number $Ro = U_\infty/(f_c D)$, where f_c is the Coriolis frequency; the stratification Froude number $Fr = U_\infty/(Nh)$, where N is the buoyancy frequency; the Reynolds number $Re = U_\infty D/\nu$. The buoyancy frequency is defined by $N^2 = -(g/\rho_0)\mathrm{d}\rho_b/\mathrm{d}z$ where ρ_b is the background density and ρ_0 is a constant reference density. We use negative Coriolis frequency ($f_c < 0$, i.e. in the Southern Hemisphere) that results in negative Rossby numbers. The Froude number is kept at $Fr = 0.15$ representing moderately strong stratification, so that most of the flow is around the obstacle. The Reynolds number is $Re = U_\infty D/\nu = 10\,000$ in the present simulation. Rotation strength is varied such that $Ro = \infty, -0.75, -0.15$, representing dynamics of non-rotational, submesoscale, and mesoscale motions. An additional induced parameter, the Burger number defined as $Bu = (Ro/Fr)^2 = (Nh/f_c D)^2$, is an important measure of the relative importance of rotation to stratification and will also be used in this work.

Figure 2 presents the visualization of the vertical vorticity (ω_z). It can be seen that stratified hill wakes are very different from their unstratified counterpart, which was studied in [6]. Being restricted by the potential energy barrier, the fluid below $O(Frh)$ from the top of the hill will

Table 1: Parameters of the simulated cases. Each case is named according to their Burger number. The number of snapshots is $N_t = 2000$, which covers more than 30 vortex shedding periods in each case.

Case	$Bu = (Ro/Fr)^2$	Ro	Fr	Re	N_t	Color
BuInf	∞	∞				red
Bu25	25	-0.75	0.15	10 000	2000	green
Bu1	1	-0.15				blue

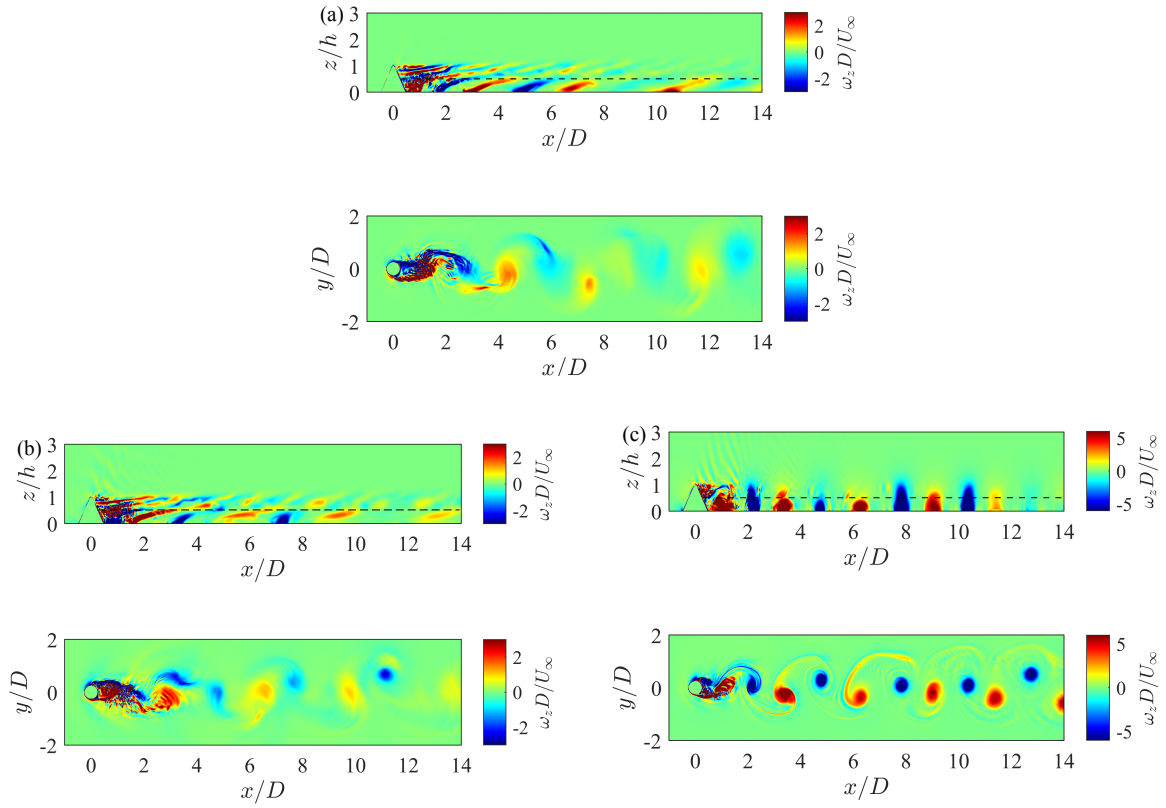

Figure 2: Flow visualizations of the vertical vorticity ω_z: (a) BuInf, (b) Bu25, (c) Bu1. Each subfigure shows ω_z on a vertical plane ($y = 0$) and on a horizontal plane ($z/h = 0.50$). Note that in (c), the magnitude of ω_z (in convective units) is much greater than in the other two cases, hence its colorbar range is different. The black dashed line in each vertical plane corresponds to $z/h = 0.50$.

not have sufficient energy to flow over the hill but can only bypass it on the sides. As a result, well-defined patterns of Kármán vortex shedding are found in horizontal planes. As the strength of rotation increases (Burger number decreases), the vertical structures of vorticity change from slanted 'tongues' to upright 'cones'.

It can also be seen that the near wake (herein $x/D < 3$) and the far wake ($x/D > 3$) exhibit different behavior. Stronger turbulence is generated near the body whereas the far wake contains predominantly coherent vortex shedding (VS) motion that persist to the end of the computational domain. It was also found that the non-hydrostatic pressure (deviation from the hydrostatic balance) is greater in the near wake and negligible in the far wake (not shown). This motivates us to separate their physics and modelling. It was found in all three cases in table 1 that there are global VS modes and a planar VS frequency that doesn't depend on vertical location [1]. This suggests a vertical correlation scale much greater than the vertical scale $U_\infty/N = 0.15h$ restricted by stratification.

In this work, we perform POD on the near and far wake of [1] separately, analyze the different limit cycles corresponding to the near and the far wake, and unveil the influence of rotation on the system. The phase portraits of POD coefficient and the correlations between planes at different heights are also studied to shed light on possible reduced-order modelling strategies.

2. Proper orthogonal decomposition

The POD problem [7, 8, 9] is to solve the following eigenvalue problem

$$\mathcal{R}\boldsymbol{\phi}_i(\boldsymbol{x}) = \int_{\mathcal{A}} \boldsymbol{R}(\boldsymbol{x},\boldsymbol{x}')\boldsymbol{W}(\boldsymbol{x}')\boldsymbol{\phi}_i(\boldsymbol{x}')\,\mathrm{d}\boldsymbol{x}' = \lambda_i\boldsymbol{\phi}_i(\boldsymbol{x}), \tag{5}$$

with $\{\boldsymbol{\phi}_i\}_{i=1}^{\infty}$ as the basis functions which are mutually orthogonal over the domain $\mathcal{A}$. Here $\boldsymbol{R}(\boldsymbol{x},\boldsymbol{x}') = \langle \boldsymbol{q}(\boldsymbol{x},t)\boldsymbol{q}(\boldsymbol{x}',t)\rangle$ is the spatial correlation tensor of a zero-mean generic signal $\boldsymbol{q}(\boldsymbol{x},t)$ and $\boldsymbol{W}(\boldsymbol{x})$ is a symmetric weight matrix that makes the following inner product,

$$(\boldsymbol{q}_1,\boldsymbol{q}_2)_{\boldsymbol{W}} = \int_{\mathcal{A}} \boldsymbol{q}_2^{\mathrm{T}}(\boldsymbol{x})\boldsymbol{W}(\boldsymbol{x})\boldsymbol{q}_1(\boldsymbol{x})\,\mathrm{d}\boldsymbol{x}, \tag{6}$$

suitable for defining an energy norm ($\|\boldsymbol{q}\|_{\boldsymbol{W}} = (\boldsymbol{q},\boldsymbol{q})^{1/2}$). Typically, $\boldsymbol{W}$ contains the constants of numerical quadrature in a discrete system.

In this work, the wake is divided into two separate regions: the near wake (A1, $x/D < 3$), and the far wake (A2, $x/D \geq 3$). The domain decomposition can be seen in figure 4. The POD problem is solved on $\mathcal{A} = \mathcal{A}_1$ and $\mathcal{A} = \mathcal{A}_2$ separately. The simulation data is arranged into

$$\boldsymbol{Q} = [\boldsymbol{q}_1, \boldsymbol{q}_2, \cdots, \boldsymbol{q}_{N_t}] \in \mathbb{R}^{N_d \times N_t} \tag{7}$$

where each $\boldsymbol{q}_i \in \mathbb{R}^{N_d}$ is one snapshot, N_d is the degree of freedom of the data, and $N_t = 2000$ is the number of snapshots. The dimension of the discrete eigenvalue problem is then $\min(N_d, N_t) = N_t$ in the present database and hence the POD is performed in the temporal domain via the method of snapshot [10].

The discrete estimate of the correlation tensor is

$$\boldsymbol{R} = \langle \boldsymbol{q}\boldsymbol{q}^{\mathrm{T}}\rangle = \frac{1}{N_t-1}\boldsymbol{Q}\boldsymbol{Q}^{\mathrm{T}} = \frac{1}{N_t-1}\sum_{i=1}^{N_t}\boldsymbol{q}_i\boldsymbol{q}_i^{\mathrm{T}} \tag{8}$$

where the factor $N_t - 1$ is the Bessel's correction such that the expectation of the sampled (co)variance converges to the (co)variance of the random signals. The discrete eigenvalue problem becomes

$$\boldsymbol{R}\boldsymbol{W}\boldsymbol{\Phi} = \boldsymbol{\Phi}\boldsymbol{\Lambda}, \tag{9}$$

or, equivalently, in the formulation of Sirovich's method of snapshots [10],

$$\frac{1}{N_t-1}\boldsymbol{Q}^{\mathrm{T}}\boldsymbol{W}\boldsymbol{Q}\boldsymbol{\Psi} = \boldsymbol{\Psi}\boldsymbol{\Lambda}, \tag{10}$$

where the POD eigenmodes are then recovered as $\tilde{\boldsymbol{\Phi}} = \boldsymbol{Q}\boldsymbol{\Psi}\boldsymbol{\Lambda}^{-1/2}$ such that the eigenfunction expansion is $\boldsymbol{R} = \tilde{\boldsymbol{\Phi}}\boldsymbol{\Lambda}\tilde{\boldsymbol{\Phi}}^{\mathrm{T}}$ with the orthogonality condition for the eigenmodes being $\tilde{\boldsymbol{\Phi}}^{\mathrm{T}}\boldsymbol{W}\tilde{\boldsymbol{\Phi}} = \boldsymbol{I}$. For convenience, the tilde will be dropped from now on. The POD expansion is then

$$\boldsymbol{q}(\boldsymbol{x},t) = \sum_{i=1}^{N_t} a_i(t)\boldsymbol{\phi}_i(\boldsymbol{x}), \tag{11}$$

where the time-dependent amplitude $a_i(t) = \sqrt{\lambda_i}\psi_i(t)$ is the rescaled eigenfunctions in the temporal domain and (11) can be regarded as either an eigen-expansion in space or in time.

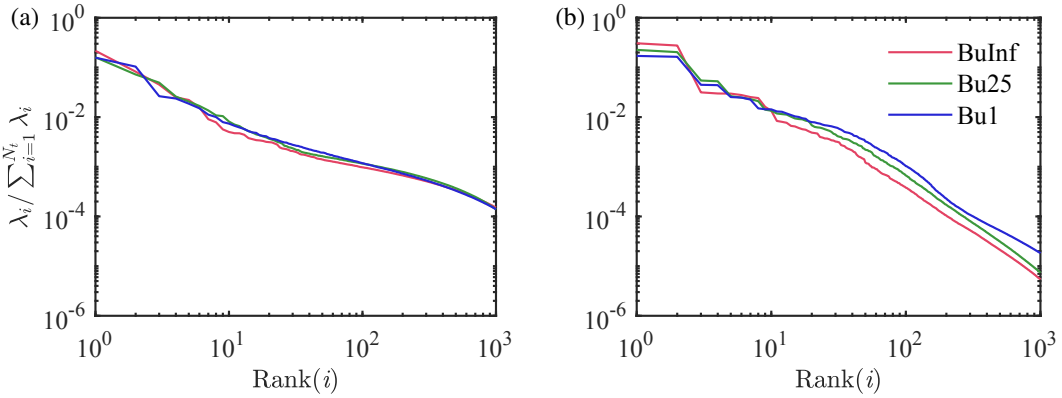

Figure 3: POD eigenspectra at $z/h = 0.25$, for BuInf (red), Bu25 (green), and Bu1 (blue): (a) the near wake; (b) the far wake. In each case and plane, the eigenvalues are normalized by the sum of all eigenvalues. The first thousand eigenvalues are shown. The first two modes account for greater than 30% of the total vertical enstrophy in all cases.

3. Results

3.1. POD eigenspectra and eigenmodes

In this work, POD is applied to the vertical component of vorticity (ω_z) in selected horizontal planes. Since the mean is removed before POD, the variance of the signal that is represented by POD is interpreted as the area integral of the fluctuation part of the vertical enstrophy ($\int_{\mathcal{A}} \omega_z'^2(\boldsymbol{x})\,\mathrm{d}\boldsymbol{x}$). Figure 3 shows the POD eigenspectra normalized by total vertical fluctuation enstrophy in near and far wakes, respectively. The spectra at different Burger numbers are quite similar, despite the increasing enstrophy in smaller scales (higher POD rank) in the far wake, as rotation strengthens (Bu decreases). POD eigenvalues are found to occur as pairs in the far wake but not in the near wake, presumably because the far wake is advection dominated and less dissipative than the near wake, and hence can be better described by travelling-wave like modes (e.g., in figure 4) that imply the degeneracy of eigenvalues. In a laminar cylinder wake, POD eigenvalues occur in pairs and the corresponding eigenmodes differ by a phase shift of 1/4 period [11, 12] in order to accommodate a travelling-wave like structure [13, 14]. However, this is not quite the case in high-Reynolds number wakes, where the second POD eigenvalue is found to be smaller than the first one [15, 16].

An example of the symmetric leading mode in case BuInf is shown in figure 4. In case BuInf, the leading modes corresponding to (a_1, a_2) are symmetric about $y = 0$ (as shown in figure 4) and leading modes corresponding to (a_3, a_4) are antisymmetric (not shown). In cases Bu25 and Bu1, the strict symmetry is broken due to the rotation but can still be found visually [1].

For all three cases and in the plane $z/h = 0.25$ as in figure 3, the first four POD modes captures 31%-36% of the variance of ω_z', and the first ten POD modes captures 38%-43%, in the near wake. The far wake shows stronger low-rank behavior that the first four modes contains 42%-64% of the variance, while the first ten contains 53%-78%. The significantly increased low-rank behavior encourages the reduced-order modelling (ROM) of the far wake.

Although the present POD does not involve all velocity components, the vorticity modes have similar shapes and wavenumbers that are shared with the velocity modes (see [17]) and are more suitable for the present problem of a well-defined vortex wake. With respect to convergence of the numerical results, the first 10 POD eigenvalues are well converged using $N_t = 400$, and the first 100 eigenvalues are converged using $N_t = 4000$. To balance efficiency and accuracy, we only analyze the first 10 POD modes and the choice of $N_t = 2000$ is sufficient.

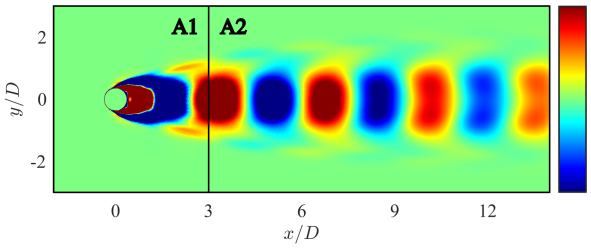

Figure 4: Leading POD modes of ω_z in the near (A1) and the far (A2) wakes pieced together, for plane at $z/h = 0.25$ in case BuInf. Note that the POD problem is solved in A1 and A2 separately, and the near wake mode is multiplied by a constant for better visual comparison.

3.2. Phase-space evolution of POD coefficients

The dynamics of wakes past bluff bodies of various cross-sections can be explained by a fixed point (mean flow) and a limit cycle around it (periodic shedding), after the first Hopf bifurcation [12, 18]. The limit cycle can be characterized by the periodic orbits of the first two coefficients of proper orthogonal decomposition (POD) modes, in wakes at Reynolds number ranging from laminar to turbulent regimes [15, 11, 12, 16, 17]. Following the framework proposed by [12], it was found in [17] that the coherent motions in the turbulent wake of a wall mounted cylinder can be well approximated by the subspace spanned by the first four POD modes. Thus, reduced order models (ROMs) of the present near and far wake are attractive. First, by comparing the leading modes measured in the far wake, it becomes possible to infer the information (such as the Rossby number which depends on the dimension of the wake generator), in an inverse problem. On the other hand, in simulations of far wakes, the time step is restricted by the fine grid near the body for a turbulence-resolving simulation and, since a substantial size of domain ($O(100D)$) is needed to reach the far wake, the computational cost becomes quite large [19, 20]. The combination of ROM (such as a Galerkin system) and broadband turbulence as a substitute inflow data generator that replaces the time-resolved near wake is appealing.

In this section, we consider the framework of Galerkin projection and it's applicability in the present flow. The time-resolved snapshots are projected on the POD modes to obtain the expansion coefficient in (11):

$$a_i(t) = \frac{(\boldsymbol{q}(\boldsymbol{x},t), \boldsymbol{\phi}_i(\boldsymbol{x}))_{\boldsymbol{W}}}{(\boldsymbol{\phi}_i(\boldsymbol{x}), \boldsymbol{\phi}_i(\boldsymbol{x}))_{\boldsymbol{W}}}. \tag{12}$$

From eqn. (11) it can also be shown that

$$\langle a_i a_j \rangle = \delta_{ij} \lambda_i, \tag{13}$$

i.e., the expected value of $\langle a_i^2 \rangle$ is λ_i. Assume the evolution of $a_i(t)$ takes the form of

$$a_i(t) = \sqrt{2\lambda_i}\cos(t), \tag{14}$$

where the factor $\sqrt{2}$ is the ratio of the maximum to the variance of a sinusoidal signal, such that the expectation of the maximum of $a_i(t)/\sqrt{2\lambda_i}$ is unity. This normalization is used for figure 5.

The trajectories of the leading pairs of POD coefficients (a_1, a_2) and (a_3, a_4) are plotted in figure 5, which are reminiscent of Lissajous curves. The trajectories of (a_1, a_i) where a_i $(i > 2)$ is any higher-rank POD coefficient are Lissajous curves with different frequency and phase relations, similar to [11, 17] and are not shown. The first few pairs (a_{2i-1}, a_{2i}) are found to be quasi-periodic in laminar and turbulent bluff body wakes [15, 11, 16, 17]. Even though each

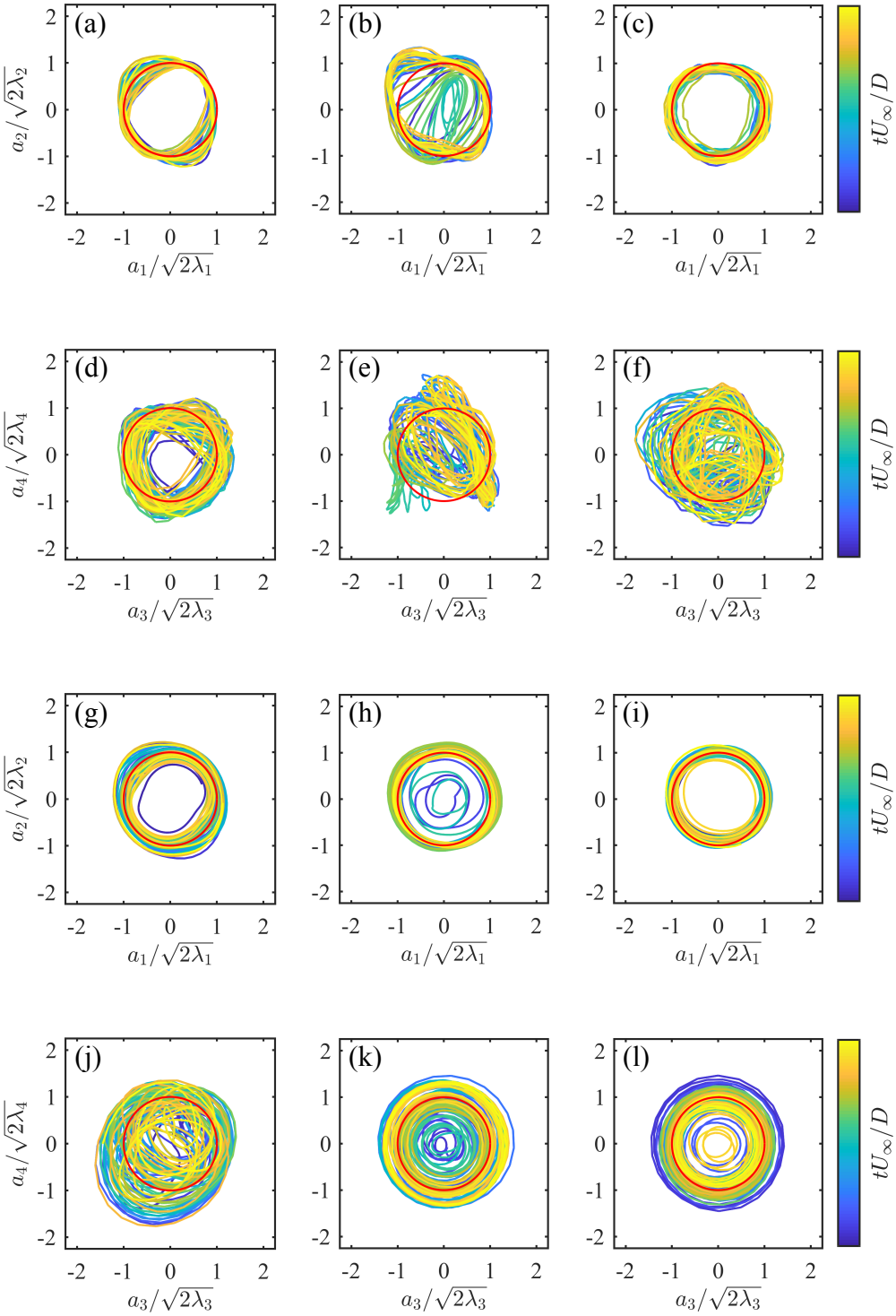

Figure 5: Trajectories of the pairs of POD coefficient (a_1, a_2) and (a_3, a_4). Left: BuInf; middle: Bu25, Right: Bu1. First two rows: near wake; last two rows: far wake. Plane locates at $z/h = 0.25$ and color denotes time (in convective units) that spans more than 30 VS cycles. The signs of a_2 and a_4 are chosen to make all the trajectories counter-clockwise. A red unit circle is also plotted as a reference.

pair of POD modes is statistically uncorrelated by construction, the members of the pair are not independent.

In figure 5, most of the trajectories are orbital while some of them are space-filling. In general, the near wake (figure 5, top two rows) is less ordered than the far wake (figure 5, bottom two rows). As the coherent VS structures emerge and dominate, the phase trajectories of both pairs of (a_1, a_2) and (a_3, a_4) approach circular orbits. Comparatively, the phase space of (a_3, a_4) is more filled than that of (a_1, a_2) for all cases, corresponding to a greater extent of variance in higher-rank modes. For the pair (a_3, a_4), although the orbits are closer to being circular going from the near to the far wake, there is still a large amplitude variation $a_3/\sqrt{2\lambda_3}, a_4/\sqrt{\lambda_4}$ ranging from 0 to about 1.5 in figure 5.

Given the nearly circular orbits of (a_1, a_2) in figure 5, and the fact that leading POD modes occur in pairs, we define the amplitude and phase of the first pair of POD modes that represent the VS motion as

$$\theta = \arctan(\frac{a_2/\sqrt{2\lambda_2}}{a_1/\sqrt{2\lambda_1}}) \tag{15}$$

$$r = \sqrt{(\frac{a_1}{\sqrt{2\lambda_1}})^2 + (\frac{a_2}{\sqrt{2\lambda_2}})^2}, \tag{16}$$

such that $(a_1/\sqrt{2\lambda_1}, a_2/\sqrt{2\lambda_2}) = re^{i\theta}$. This POD phase is found to agree well with the phase identified from the pressure signals [21]. Both θ and r will be analyzed in detail in a later section.

3.3. Inter-plane correlation between POD coefficients

With the aim of understanding the inter-plane connection that could be helpful in the modelling such flows, we study the correlations between POD coefficients and amplitudes. As seen in the previous section, the first two POD coefficients (a_1 and a_2) are not independent, and represent the same dynamics of VS motion. Hence, we only analyze the inter-plane correlation of a_1 in this section. The correlation of a_1 at two different heights is defined as

$$C_1(\Delta t; z_1, z_2) = \frac{\langle a_1(t; z_1) a_1(t + \Delta t; z_2)\rangle}{\langle a_1(t; z_1)^2\rangle^{1/2} \langle a_1(t; z_2)^2\rangle^{1/2}}, \tag{17}$$

where z_1, z_2 are the distance from the bottom wall. Since $C_1(\Delta t) \neq C_1(-\Delta t)$ in general, we require the order of $z_1 < z_2$. Moreover, the value of $C_1(0; z_1, z_2)$ can be used to evaluate the phase lag between two planes, assuming that both are evolving at the same frequency. Assume two harmonic signals in $[0, 2\pi]$

$$q_1(t) = \sin t,\ q_2(t) = \sin(t + \psi) \tag{18}$$

share the same frequency but only differ by a phase shift. Their correlation at $\Delta t = 0$ is

$$C_q = \frac{\langle q_1 q_2\rangle}{\langle q_1^2\rangle^{1/2} \langle q_2^2\rangle^{1/2}} = \frac{\langle \frac{1}{2}\cos\psi - \frac{1}{2}\cos(2t + \psi)\rangle}{\frac{1}{\sqrt{2}}\frac{1}{\sqrt{2}}} = \cos\psi, \tag{19}$$

which only depend on the phase difference (ψ) between these two signals. Here $\langle\cdot\rangle$ is interpreted as $1/(2\pi)\int_0^{2\pi} \mathrm{d}t$. If q_1 and q_2 are in phase ($\psi = 0$) then $C_q(0) = 1$ is true.

Figure 6 compares the correlation (17) between the near and the far wake. The pairs of planes are taken from $z/h = 0.12, 0.25, 0.50, 0.75$. The correlation coefficients are harmonic, with the period being close to the VS period ($T_{\mathrm{VS}} \approx 4D/U_\infty$), but the maximum can vary. A harmonic correlation function with a maximum close to unity indicates that the POD modes of different planes oscillate at the same frequency but only with a phase shift. This is the case in figure 6.

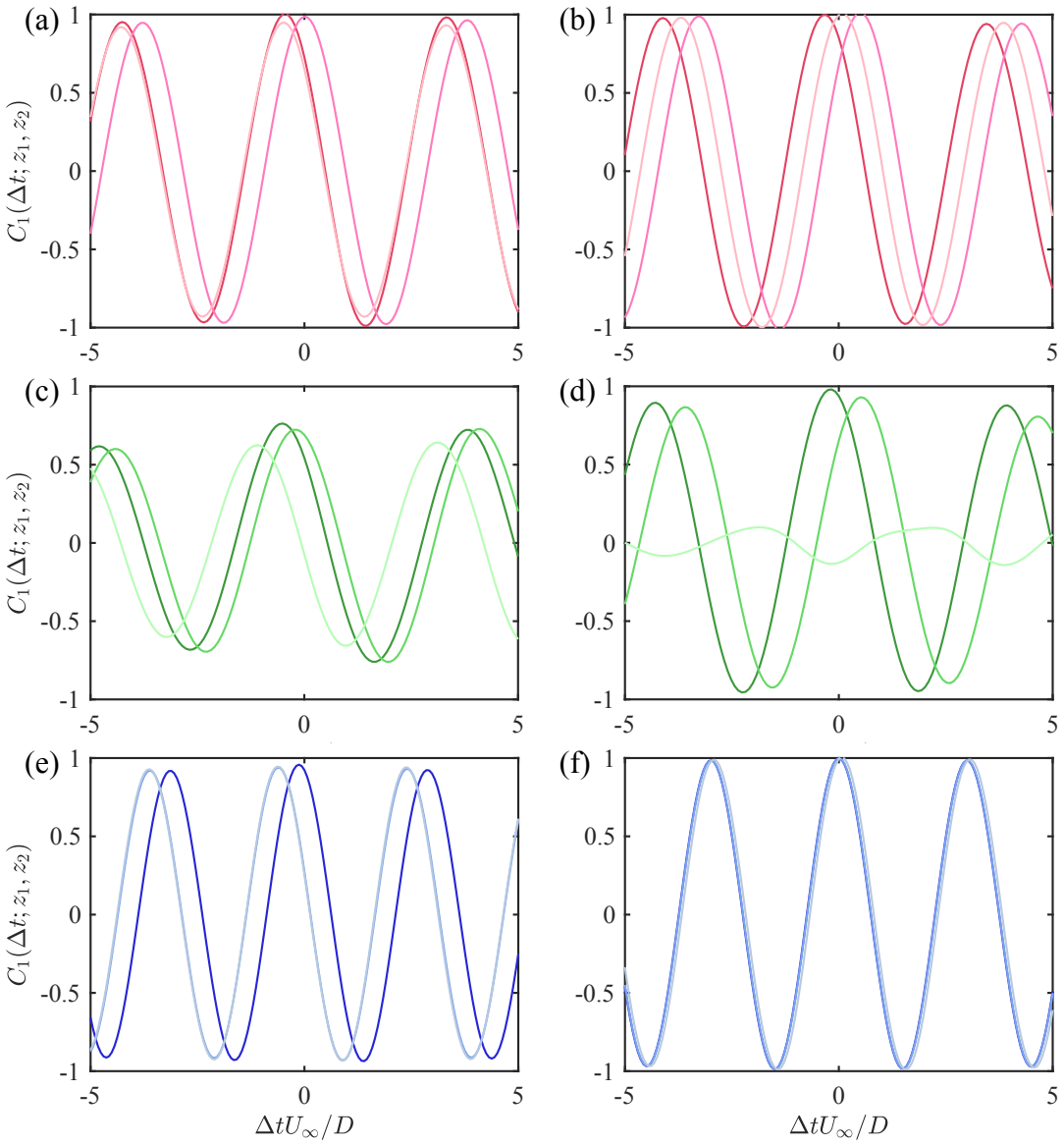

Figure 6: POD correlation coefficients $C_1(\Delta t; z_1, z_2)$ of the first mode at two different planes. (a,c,e) show the near wake (A1) and (b,d,f) show the far wake (A2). (a,b) BuInf; (c,d) Bu25; (e,f) Bu1. Colors from dark to light indicate pairs of planes at $(z_1/h, z_2/h) = (0.12, 0.25), (0.12, 0.50), (0.12, 0.75)$.

For case BuInf, both the correlations in the near and the far wake achieve the maximum close to unity, indicating that a constant VS frequency is maintained both in the near and the far wake but the phase lag between different planes has change a bit.

The correlations in case Bu1 are similar to BuInf in the near wake, both in terms of phase lag and maximum. However, the far wake in case Bu1 shows exactly the same phase in the four planes examined, as implied by $C_1(0; z_1, z_2) = 1$ and according to (19). This is in agreement with the vertically aligned vortex 'columns' shown in figure 2(c) where the VS in each height are in phase. The simpler vertical structures in the strongly rotating case Bu1 implies the possibility of neglecting the inter-plane phase difference of VS when modelling is considered.

Contrary to BuInf and Bu1, the inter-plane correlation in case Bu25 is larger in the far wake

than in the near wake, except for the farthest pair $z/h = (0.12, 0.75)$. This increased degree of order is consistent with the phase portraits of (a_1, a_2) and (a_3, a_4) (middle column of figure 5) which are more regular in the far wake. Additionally, as shown in figure 6(d), the first POD mode at $z/h = 0.75$ in case Bu25 is hardly correlated to that at $z/h = 0.12$. This doesn't indicate a complete loss of vertical coherence at $z/h = 0.75$ but is a result of mixed frequencies in POD modes. A spectral POD analysis which separates structures that oscillate at different frequencies was performed in [1] and the dominant mode in that plane is still the VS mode at the VS frequency, and the three-dimensional coherent VS structures are found to extend vertically beyond $z/h = 0.75$. In all, the difference observed in Bu25 implies a non-monotonic dependence of wake coherence on rotation, which needs to be accounted for in any modeling strategies.

From figure 6, it can be inferred that the correlation coefficients can generally achieve a value of nearly unity for a certain time lag Δt between two planes separated at $z_1/h = 0.12$ and $z_2/h = 0.75$, suggesting that the flow remains coherent in this range. Note that the uppermost and lowermost planes ($z/h = 0.12$ and $z/h = 0.75$) are chosen to be the rough boundaries of the core of the vortex wake - neither too close to the top of the hill to be influenced by internal gravity waves nor in the bottom boundary layer where the wake is disturbed. This gives some hope that the core of the wake - isolated from the obstacle as well as the bottom wall - can be described with a ROM.

In all cases, the maximum location of $C_1(\Delta t) = 1$ nearest to $\Delta t = 0$ tend to be negative in the near wake. Combining with (17) and the fact that $z_1 < z_2$, it implies that the upper planes lead in the phase, consistent with figure 2 and the global modes in [1]. The phase of each plane will be further analyzed in the next section.

3.4. Analysis of the phase and the amplitude of the VS mode

In order to model these wakes by assuming periodic base flow in the form of periodic VS motions in each plane with a phase shift between planes, one needs to know whether constant VS frequency and phase lag are maintained throughout the evolution. Also, the variability of the amplitude r of the periodic leading mode $a_1\boldsymbol{\phi}_1 + a_2\boldsymbol{\phi}_2$ is important to modelling. Besides, as shown in figure 5, the variation of the amplitude of the leading modes during their evolution is not negligible. The correlation between amplitudes at two offset planes would be of interest as it gives an idea as to how much the knowledge in one plane can be used to infer another and whether this system can be further reduced. In this section, the phase θ and amplitude r of the orbital motion of (a_1, a_2), defined in (15), will be analyzed.

Figure 7(a) shows the phase angle of the leading pair defined in (15) in the far wake as a continuous function of time. The angle is allowed to exceed 2π as more cycles elapse. The slopes give an estimate of the averaged VS Strouhal number $St_{\mathrm{VS}} \approx 0.26$ in all three cases, and the VS frequency is quite constant during the evolution, for all cases (excluding $z/h = 0.75$ in Bu25 that will be discussed below).

For case Bu25 (figure 7c), the phase angle in plane $z/h = 0.75$ varies significantly from others, and leads to a frequency almost twice of the shedding frequency. This is due to the fact that in this case the f-k_x relation of the POD modes is not linear, or in other words, there are mixed frequencies. Here f and k_x are the dominant frequency and streamwise wavenumber of a POD mode, respectively. In cylinder wakes [11, 12] or the present hill wake [1] the relation between f and k_x is quite linear - a pair of POD modes will have a single characteristic streamwise wavenumber and a single frequency of associated coefficients. For example, the first pair has a wavelength $k_x = 2\pi/\lambda_x$ (λ_x is the average separation between same-sign vortices) and evolves at f_{VS}, and the second pair has a wavelength $2k_x$ and evolves at $2f_{\mathrm{VS}}$, and so forth. This is found to be true in the present wake (except for $z/h = 0.75$, case Bu25) for at least the best-resolved first 6 POD modes. This linear relation results in the same spatial modes if the spectral POD (SPOD) is carried out at the first 3 frequencies - $f_{\mathrm{VS}}, 2f_{\mathrm{VS}}, 3f_{\mathrm{VS}}$. In case Bu25, where the first

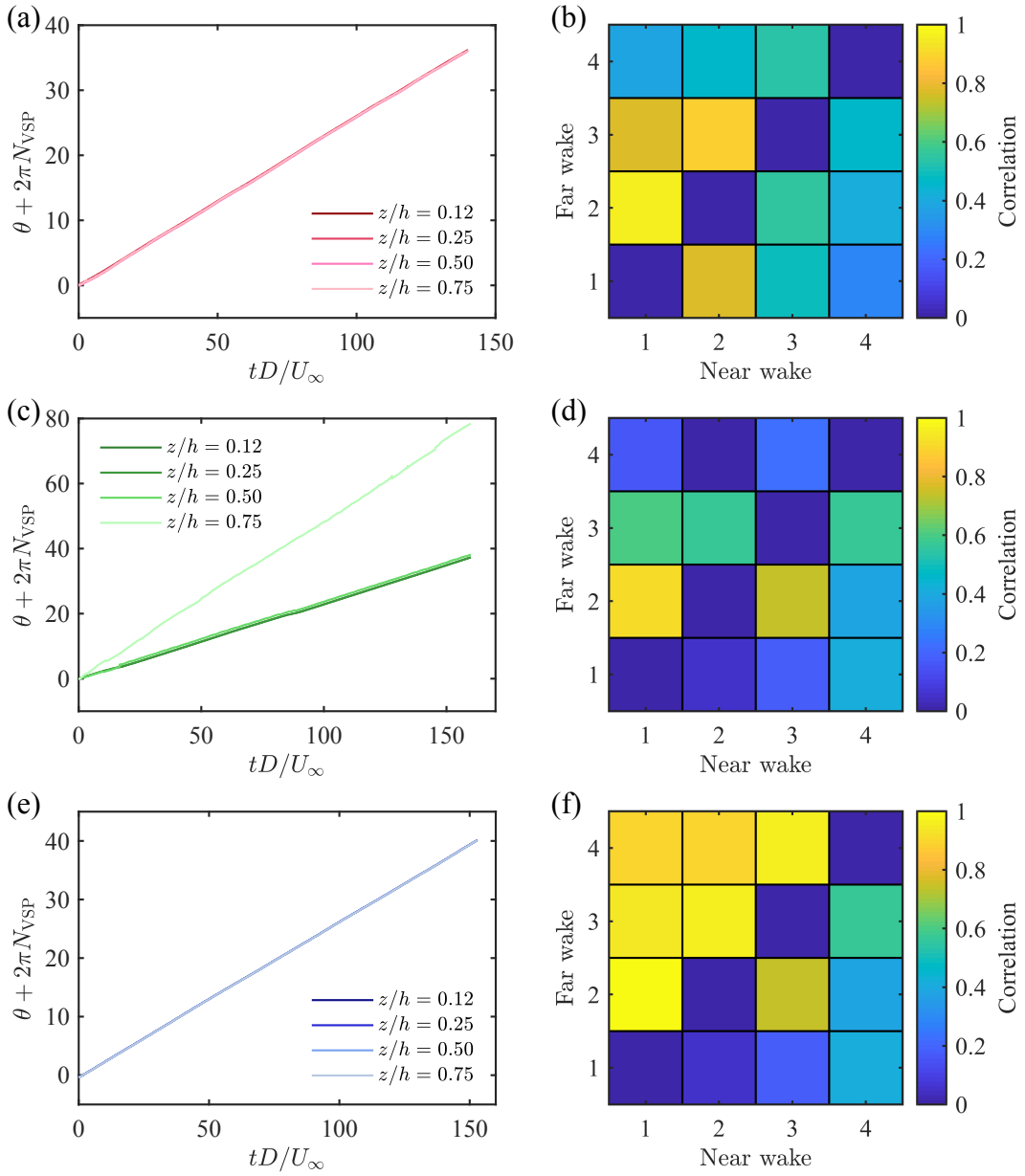

Figure 7: (a,c,e) The POD phase angle θ as a function of time, in the far wake. The phases are shifted to be continuous by adding integer multiples of the VS period (VSP). (b,d,f) Coherence map in the near wake and in the far wake. Cases Buinf (a,b), Bu25 (c,d), and Bu1 (e,f). Color represents correlation coefficient $C_r(\Delta t_{\max}; z_1, z_2)$ between two planes, where $z_1 < z_2$ and $\Delta t_{\max}$ is the optimal time lag between two planes that maximizes the correlation coefficient. The elements below the diagonal line are for the near wake, while those above are for the far wake. Elements on the diagonal line representing self-correlation which are expected to be unity are removed for clarity. Numbers from 1 to 4 represent planes at $z/h = 0.12, 0.25, 0.50, 0.75$.

4 POD modes all have the same wavelength (not shown) and similar shapes with a tendency to symmetry about $y = 0$ (not shown), hence the second harmonic ($2f_{\mathrm{VS}}$) is aliased to the projection coefficient of the first pair of POD modes. The preceding argument explains the anomalous slope in figure 7(c) and the low amplitude of the correlation function in figure 6 in the $z/h = 0.75$ plane. A SPOD analysis in [1] which is advantageous over POD in this special situation ascertains that the dominant frequency of this plane is still the same as other planes (f_{VS}).

The correlations between the amplitude of the first pair POD modes (defined in (17)) at two different planes are compiled into correlation maps in figure 7(b,d,f). A unit amplitude of r is regarded as a baseline of the model periodic flow $(a_1, a_2) = re^{i\theta}$ and is subtracted. We denote the deviation of r from unity as $r' = r - 1$ and similar to (17), the correlation between the values of r' in two different planes is denoted as $C_r(\Delta t_{\max}; z_1, z_2)$. The optimal time lag $\Delta t_{\max}$ that maximizes $C_r(\Delta t; z_1, z_2)$ differs among cases. To take advantage of the symmetry with respect to the commutation of z_1 and z_2, C_r in the near wake and the far wake are plotted in the lower and upper triangles of the matrices in figure 7, respectively, for better comparison. The matrices are colored according to the magnitudes of correlation coefficients. Here we use 1 to 4 to refer to planes from bottom to top.

In case BuInf, it can be seen that planes 1 and 2 have the strongest correlation in the near wake, while this correlation is strengthened in the far wake, accompanied by the increased correlation between planes 1, 3 and 2, 3. This also implies an emergence of order during the evolution. No matter in the near or in the far wake, the topmost plane 4 at $z/h = 0.75$ is not well correlated with others. In case Bu25, there is only one strong correlation in the near and in the far wake, respectively. And all planes are mutually less correlated for Bu25 compared to the other two cases. In case Bu1, there is only one pair of planes that have a correlation greater than 0.6 in the near wake. However, when the flow enters the far wake, the magnitudes show that all planes become correlated mutually, suggesting the best vertical coherence in this case and significant simplification in its modelling.

4. Summary and conclusions

Geophysical wakes visually exhibit coherent eddies in their horizontal motion (coherent vertical vorticity ω_z) as is well known from satellite and other images of cloud cover and ocean color. Less known is the systematic influence of density stratification and rotation on the dynamics of these wake eddies. Thus motivated, we conduct POD analysis of a time-resolved wake dataset. The specific problem is a steady current past a conical obstacle - a hill or seamount - with 30° slope and $Re = U_\infty D/\nu = 10\,000$. Unstratified flow past a conical obstacle does not exhibit coherent ω_z eddies. The stratification, which has to be sufficiently large for flow to be primarily around the obstacle than over it, is chosen so that the height-based Froude number is $Fr = U_\infty/Nh = 0.15$. System rotation is systematically increased from the non-rotating case to values corresponding to Rossby number $Ro = U_\infty/fD = -0.75$ and $Ro = -0.15$. The negative value of Ro follows from the chosen Southern Hemisphere location with negative (clockwise) rotation and Coriolis frequency (f_c). Associated with the change of rotation rate at fixed stratification, the Burger number $Bu = (Ro/Fr)^2$ (a measure of the relative strength of stratification to rotation) takes the values of ∞ (case BuInf), 25 (case Bu25) and 1 (case Bu1) corresponding to $Ro = \infty$, -0.75 and -0.15, respectively.

POD is the tool employed here to diagnose coherent dynamics in the simulated wakes with a focus on the effect of system rotation. POD is conducted on the vertical vorticity at selected horizontal planes ($z/h = 0.12$, 0.25. 0.5 and 0.75) chosen to encompass the wake core, away from the bottom boundary layer and also from the upper region with internal gravity waves. The leading members of the set of POD coefficients $\{a_i(t)\}$ are investigated and their cross-correlation between planes at different elevations is computed to reveal inter-plane coherence.

The near wake ($x/D < 3$) has turbulence and also interacts with internal waves. Therefore, the near and far wakes are analyzed separately.

Vortex shedding at a specific frequency and advection of the vortices by a constant speed would lead to a limit cycle in the trajectory of $a_2(t)$ plotted against $a_1(t)$. The expectation that an increase of rotation rate (decreasing $|Ro|$ and decreasing Bu) would lead to a *systematic* increase of coherence as measured by POD is *not* borne out. The overarching conclusion of the POD analysis is that the dependence is more complex as summarized and discussed below.

For the near wake, trajectories in $a_1(t), a_2(t)$ coordinates show that there is a *decrease* in coherence relative to the baseline non-rotating case when $|Ro|$ decreases to 0.75 (case Bu25) followed by an increase when $|Ro|$ decreases to 0.15 (case Bu1). In particular, the trajectories in case Bu25 (see figure 5b) are space-filling rather than repeating on an orbital path. Since $Ro = -0.75$ is in the submesoscale regime, the newly-formed vortices can be unstable to submesoscale instabilities that are known to occur at $Ro = O(1)$ and cause deviations from a defined orbit. For the far wake, it is the cases $Bu = 25, 1$ with rotation that display more ordered trajectories while the non-rotating case (BuInf) show more variance.

The inter-plane cross-correlation coefficient $C_1(\Delta t; z_1, z_2)$ is also computed to diagnose correlation across planes at different elevations. The characteristic vertical scale is U/N which, when nondimensionalized by h becomes $Fr = U_\infty/Nh$ and takes the value of 0.15 in all cases. The correlation between the VS modes in different horizontal planes can stay correlated with a vertical separation several times greater than the stratification length scale for overturn motions (U/N), as can be seen in figure 6. The vertical coherence and temporal periodicity of vortex motions encourages the ROM of such wakes. The simplest model of the leading POD coefficients that is consistent with vortex shedding is a limit cycle with frequency that is constant across z_1 and z_2. Such a model would lead to $C_1(\Delta t; z_1, z_2)$ taking the form of a harmonic function with unity amplitude. Indeed, the non-rotating, strongly-stratified case BuInf and the strongly-rotating, strongly-stratified case Bu1 do conform to the simple model in both the near and the far wake. It is intermediately strong rotation that breaks this model. At $Ro = -0.75$ (Bu25), the behavior is that of a harmonic function but with amplitude reduced from 1 to about 0.6 in the near wake. The amplitude recovers to near unity in the far wake except for the $(z_1 = 0.12, z_2 = 0.75)$ pair which includes planes at the upper and lower edges of the wake core.

A correlation map (figure 7, right column) summarizes inter-plane correlation. It is evident that as the flow progresses from the near to the far wake there is a strong increase in mutual correlation, i.e., a significant increase in order. We conclude that ROM could provide a possible surrogate for the coherent part of wake dynamics and also as part of the inflow generation procedure for more complex problems, e.g., the interaction of wake vortices with downstream features such as broad-band roughness, other isolated topographic elements, a different stratification, etc. A caveat is that, at the large Re of geophysical flows, additional modeling would be needed for the incoherent part and its potential feedback to the low-order model. Furthermore, it is quite possible that, at even stronger stratification and values of Fr less than 0.15, the inter-plane coherence of wake eddies would be disrupted [22].

Acknowledgements
The authors would like to acknowledge the financial support from ONR grant N00014-22-1-2024. This work was also supported by the European Research Council under the advanced grant ERC-AdG-101018287 ('CausT') during the stay of J. L. in the fifth Madrid turbulence summer school, for which the hospitality by the Fluid Dynamics Group at Universidad Politécnica de Madrid is gratefully acknowledged. We especially thank Scott Dawson and Barbara Lopez-Doriga from Illinois Institute of Technology for reviewing the draft of this paper.

References

[1] Liu J, Puthan P and Sarkar S 2023 *to appear on arXiv*
[2] Nicoud F and Ducros F 1999 *Flow, Turbulence and Combustion* **62** 183–200
[3] Balaras E 2004 *Computers & Fluids* **33** 375–404
[4] Yang J and Balaras E 2006 *Journal of Computational Physics* **215** 12–40
[5] Puthan P, Jalali M, Ortiz-Tarin J L, Chongsiripinyo K, Pawlak G and Sarkar S 2020 *Ocean Model.* **149** 101611
[6] Garcia-Villalba M, Li N, Rodi W and Leschziner M 2009 *J. Fluid Mech.* **627** 55–96
[7] Lumley J L 1967 *Atmospheric turbulence and radio wave propagation* 166–178
[8] Lumley J L 1970 *Stochastic tools in turbulence* (Academic Press)
[9] Holmes P, Lumley J L, Berkooz G and Rowley C W 2012 *Turbulence, Coherent Structures, Dynamical Systems and Symmetry* 2nd ed (Cambridge university press)
[10] Sirovich L 1987 *Quarterly of applied mathematics* **45** 561–571
[11] Ma X and Karniadakis G E 2002 *J. Fluid Mech.* **458** 181–190
[12] Noack B R, Afanasiev K, Morzyński M, Tadmor G and Thiele F 2003 *J. Fluid Mech.* **497** 335–363
[13] Rempfer D and Fasel H F 1994 *J. Fluid Mech.* **260** 351–375
[14] Taira K, Brunton S L, Dawson S T, Rowley C W, Colonius T, McKeon B J, Schmidt O T, Gordeyev S, Theofilis V and Ukeiley L S 2017 *AIAA J.* **55** 4013–4041
[15] Ma X, Karamanos G S and Karniadakis G 2000 *J. Fluid Mech.* **410** 29–65
[16] Oudheusden B v, Scarano F, Hinsberg N v and Watt D 2005 *Experiments in Fluids* **39** 86–98
[17] Bourgeois J, Noack B and Martinuzzi R 2013 *J. Fluid Mech.* **736** 316–350
[18] Barkley D 2006 *Europhys. Lett.)* **75** 750
[19] VanDine A, Chongsiripinyo K and Sarkar S 2018 *Computers & Fluids* **171** 41–52
[20] Ortiz-Tarin J, Nidhan S and Sarkar S 2021 *J. Fluid Mech.* **918** A30
[21] Perrin R, Braza M, Cid E, Cazin S, Barthet A, Sevrain A, Mockett C and Thiele F 2007 *Exp. Fluids* **43** 341–355
[22] Perfect B, Kumar N and Riley J 2018 *Geophysical Research Letters* **45** 9098–9105